

Hall-Bulk photovoltaic effect in BiFeO₃/SrTiO₃ at low temperatures

Hang-Bo Zhang ¹✉ & Marin Alexe ¹✉

The bulk photovoltaic effect is considered promising for the next generation of solar cells as it could exceed the Shockley-Queisser limit. Studies have shown many materials have the bulk photovoltaic effect, however, the inner properties such as carrier mobility, relaxation time, etc., have been barely reported, largely hindering further understanding and utilization of the bulk photovoltaic effect. In this paper, we employ a Hall effect to study the transport properties of the bulk photovoltaic effect in a BiFeO₃/SrTiO₃ heterostructure. We interpret the magnetic field-dependent bulk photovoltaic currents using the fundamental Lorentz force law acting on photocarriers. A carrier transport with ~3 ps relaxation time, a mobility of $3.3 \times 10^3 \text{ cm}^2 \text{ V}^{-1} \text{ s}^{-1}$ for the non-thermalised carrier and a mean free path larger than 50 nm are revealed. This is in good agreement with the ballistic transport mechanism. This work provides a generic approach to acquiring the basic characteristics of the bulk photovoltaic effect.

¹Department of Physics, the University of Warwick, Gibbet Hill Road, Coventry CV4 7AL, UK. ✉email: hangbozhang@outlook.com; M.Alexe@warwick.ac.uk

The bulk photovoltaic (BPV) effect, a nonlinear photo-response to the polarised light, can generate a directional photocurrent under uniform illumination in most non-centrosymmetric materials^{1,2}. This photovoltaic effect is not based on a gradient in quasi-Fermi levels, as in classical semiconductor photo-cells, so it should in principle not suffer from the Shockley-Queisser limit³. However, the light energy conversion efficiency of the photovoltaic devices based on materials that are innate non-centrosymmetric (polar materials), such as ferroelectrics, is usually very limited^{3,4}.

To boost the power conversion efficiency of the BPV effect in a certain material, it is important to understand fundamental optoelectronic processes such as carrier generation, transport, and recombination^{5,6}. One good example of exploiting the optoelectronic process to enhance the BPV effect is given by Zenkevich et al.⁷. It was demonstrated that by engineering the film thickness to be comparable with the photocarriers thermalisation length, the photovoltaic effect of the respective thin film was largely improved. However, to date, very few reports have so far addressed the fundamental electronic process of the BPV effect.

The magnetic field-dependent photoelectric effect might be the ideal experimental way to address this problem^{8,9}. Under the application of a magnetic field, the photocurrent experiences a Lorentz force and thus the fundamental carrier transport properties can be unveiled. Previous reports have employed the Hall effect to investigate the response of the BPV behaviour to the magnetic field^{10–12}. However, these experiments only involved the photocurrent behaviour at a fixed light polarisation, therefore, could not give a full profile of BPV behaviours in the magnetic field. In this work, we demonstrate the evolution of the BPV currents of BiFeO₃/SrTiO₃ (BFO/STO) in the presence of a magnetic field. We give clear evidences that the Hall effect dominates the magnetic field-dependent BPV behaviours at low temperatures. Our analysis shows that the BPV effect of BFO/STO has a high non-thermalised carrier mobility and a long mean free path, belonging to the ballistic mechanism.

Results and discussion

Photocurrent measurement. We mainly focus on the Hall effect on the BPV behaviour in a well-studied system BFO/STO. The (~200 nm) BFO thin film was epitaxially grown on (001)-oriented STO single crystal substrates in special conditions to yield the single-crystal monodomain structure with C_{3v} point group symmetry¹³. Photo-Hall characterisations were performed by applying a magnetic field normal to the film plane, illuminating the sample with polarised light, and collecting photocurrents in two orthogonal directions. The experimental setup is schematically illustrated in Fig. 1a, where a half-wave plate (HWP) is used to modulate the polarisation of the 405 nm laser beam to measure the linear BPV current. The detail of the experimental setup and the related piezoresponse force microscopy studies of the thin film are given in Supplementary Fig. 1.

The BPV currents were confined to the film plane, the directions of which are defined according to the film-plane projection of the ferroelectric polarisation P^{FP} as marked in Fig. 1a. According to phenomenological theory and the geometry of the experimental setup, the HWP angle-resolved BPV currents without any magnetic field can be simply written as^{1,13}

$$J_x = A_x \sin(4(\theta + \theta_x)) \quad (1)$$

$$J_y = A_y \sin(4(\theta + \theta_y)) \quad (2)$$

where J_x and J_y are the photocurrent along the lab coordinate x and y , respectively; A_x (A_y) is the sine photocurrent amplitude of J_x (J_y), θ is the HWP angle; θ_x (θ_y) is the initial BPV angle offset of

J_x (J_y). It is worth noting that the light polarisation-independent photocurrent background (offset) is not the main focus here, as it may also comprise other contributions that are irrelevant to the BPV effect.

It has been demonstrated that the photocarrier mobility in a BFO/STO system can be very high at their interface due to the nature of STO¹⁴. This is more significant when the temperature is lower than 30 K, as the carrier mobility of STO can go to $10^3 \text{ cm}^2 \text{ V}^{-1} \text{ s}^{-1}$ due to the nature of STO¹⁵. To build the temperature-dependent correlation between carrier mobility and the Hall-effect behaviour, we conducted the experiments in the temperature range from 70 K to 10 K. The BPV currents J_x as a function of the HWP angle at the different magnetic fields of -3 T , 0 T , and 3 T are present in Fig. 1b–g. Initially, at 70 K, the BPV current was nearly insensitive to the applied magnetic field. However, by lowering the temperature to 50 K, we observed an obvious change in the photocurrent amplitude due to the application of the magnetic field. By further lowering the temperature to 30 K and below, a significant BPV angle shift was additionally determined. We found that the photovoltaic current changes sign when the temperature decreases from 40 K to 30 K and below. As has been analyzed in our previous work showing that STO contributes significantly to the BPV effect at low temperatures¹⁴. As shown in Supplementary Fig. 2, there change in the BPV effect at temperatures below 40 K. This is a clear indication that the BPV effect has now a large contribution from STO (more details are given in Supplementary Note 2 and Supplementary Fig. 2).

The above magnetic field-dependent BPV results reveal that a significant influence of the applied magnetic field on the BPV effect is sizable at about 40–50 K and lower mainly due to the STO part of the thin film. To establish the landscape of the magnetic-field dependent BPV, we measured both BPV currents J_x and J_y under the magnetic field in a wide range between -6 T and 6 T , the detail of which is given in Supplementary Note 3 and Supplementary Fig. 3.

Magnetic field-dependent BPV properties. In order to quantify the effect of the magnetic field on the BPV currents, we add the magnetic field dependence of the BPV current amplitude and angle into Eqs. 1 and 2. The expressions of BPV currents in a magnetic field are:

$$J_x^B = A_x^B \sin(4(\theta + \theta_x^B)) \quad (3)$$

$$J_y^B = A_y^B \sin(4(\theta + \theta_y^B)) \quad (4)$$

where the superscript B indicates the magnetic field dependence. The magnetic field-dependent BPV amplitude and angle are consequently obtained via fitting the sine HWP angle-dependent photocurrents with a least-square fitting method. The BPV angle shift $\Delta\theta_x^B$ and $\Delta\theta_y^B$ compared to the pristine state and a rescaled BPV amplitude is used to better understand the change in the BPV current. The results shown in Fig. 2a, b clearly demonstrate that the BPV angle is magnetic-field- and temperature-dependent. In both photocurrent directions, the BPV angles shift monotonically from the negative to positive magnetic field only below 30 K, remaining nearly unchanged at temperatures above 60 K. Compared to the BPV angle, the BPV amplitudes show more intricate magnetic field behaviours. Nevertheless, the dependence of the BPV amplitudes on the magnetic field is also largely reduced when the temperature is higher than 60 K.

The above results indicate that the magnetic-field dependence of the BPV effect is strong at low temperatures, directly pointing out that it is the STO playing a decisive role, as we know that BFO exhibit a depressed photo-response at low temperatures^{13,16}. Carrier mobility of STO sharply increases when the temperature

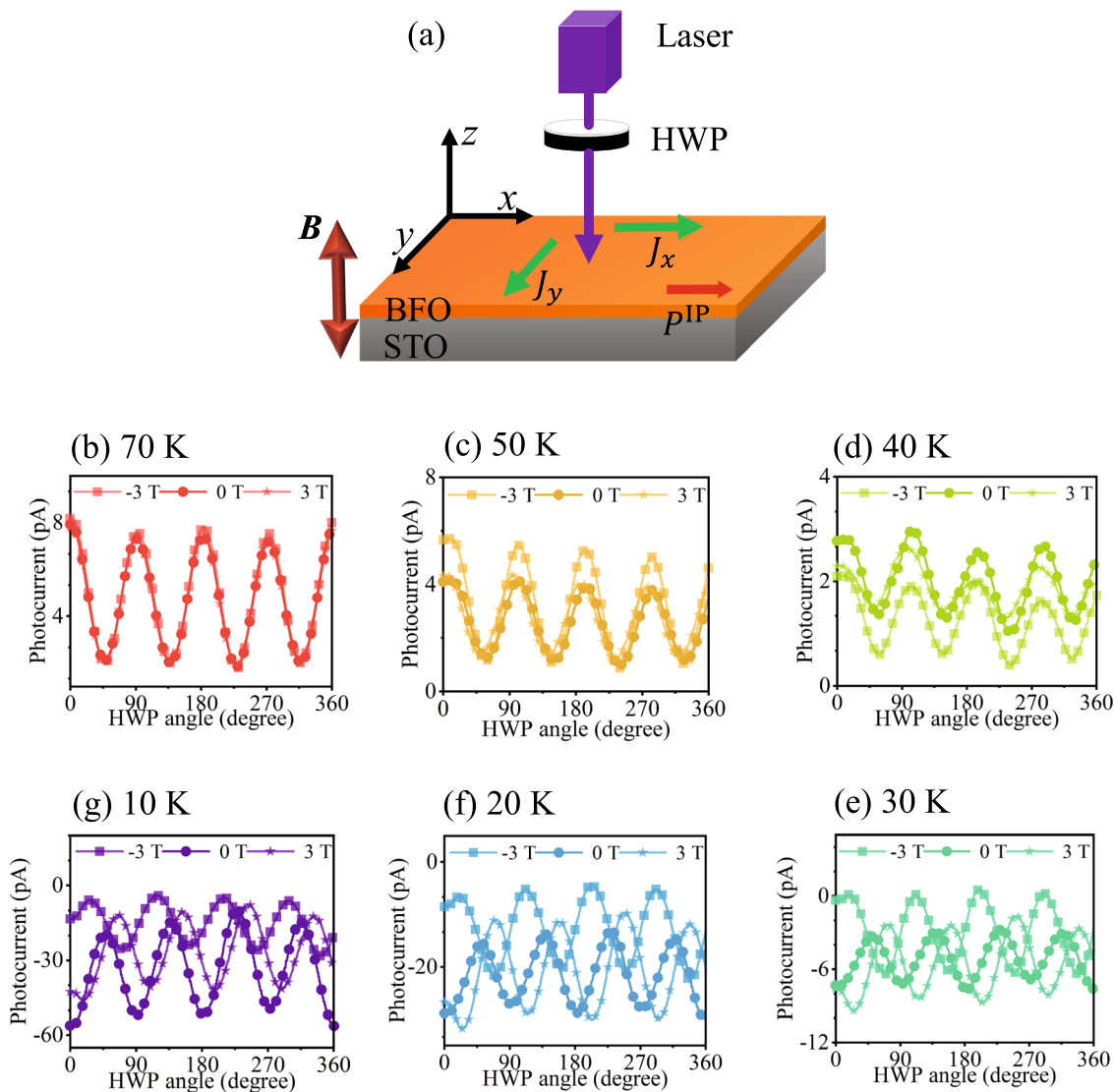


Fig. 1 Experimental setup and bulk photovoltaic (BPV) currents at different temperatures under a magnetic field. **a** Schematic of the experimental setup for the measurement of the BPV effect in BiFeO₃/SrTiO₃ (BFO/STO) under a magnetic field \mathbf{B} (deep red arrow) normal to the film plane. The Photocurrents, indicated by the green arrow, are collected along either x direction (J_x) or y direction (J_y); the in-plane ferroelectric polarisation of BFO (P^{IP}) is parallel to the x direction as indicated by the red arrow. A half-wave plate (HWP) was used to modulate the light polarisation. **b–g** HWP angle-resolved photocurrent J_y at different temperatures under magnetic fields of -3 T, 0 T, and 3 T. Detailed descriptions are given in the ‘Photocurrent measurement’ section.

drops below 30 K. Therefore, under the magnetic field a similar effect to a Hall effect changes the photocarrier transport path within the collection of the electrodes.

Macroscopic analysis: a Hall-effect study. Before further analysing the Hall-like effect on the BPV response, we first verify another geometry where the magnetic field is parallel to the film plane (Supplementary Note 4 and Supplementary Fig. 4). With this setup, one photocurrent is now perpendicular to the magnetic field and another one is parallel to the magnetic field. In principle, if the Hall effect dominates the magnetic field-dependent BPV current, the photocurrent along the magnetic field will not be changed. In turn, the photocurrent perpendicular to the magnetic field will be changed upon the application of the magnetic field. Our results displayed in Supplementary Fig. 4 give clear evidence to support our assumption and thus confirm the existence of the Hall effect on the BPV current.

Based on the above results, we now consider the photocurrent trajectory is deflected by the Lorentz force. To illustrate this process, the total BPV current is decomposed in two orthogonal directions, i.e., J_x and J_y . The values given by Eqs. 1 and 2 are the original states (see Fig. 3a).

After applying a magnetic field, the BPV currents are effectively rotated by a certain angle in the film plane due to the Lorentz force and expressed as J_x^B and J_y^B . The characteristics of the new BPV currents, i.e., the amplitudes and angles remain identical as the magnetic field does not change the material symmetry. The rotated BPV currents have two projections on the x - and y -axis and now are expressed as:

$$J_x^{x,B} = \Delta_x^{x,B} J_x^B = \Delta_x^{x,B} A_x \sin(4(\theta + \theta_x)) \quad (5)$$

$$J_x^{y,B} = \Delta_x^{y,B} J_x^B = \Delta_x^{y,B} A_x \sin(4(\theta + \theta_x)) \quad (6)$$

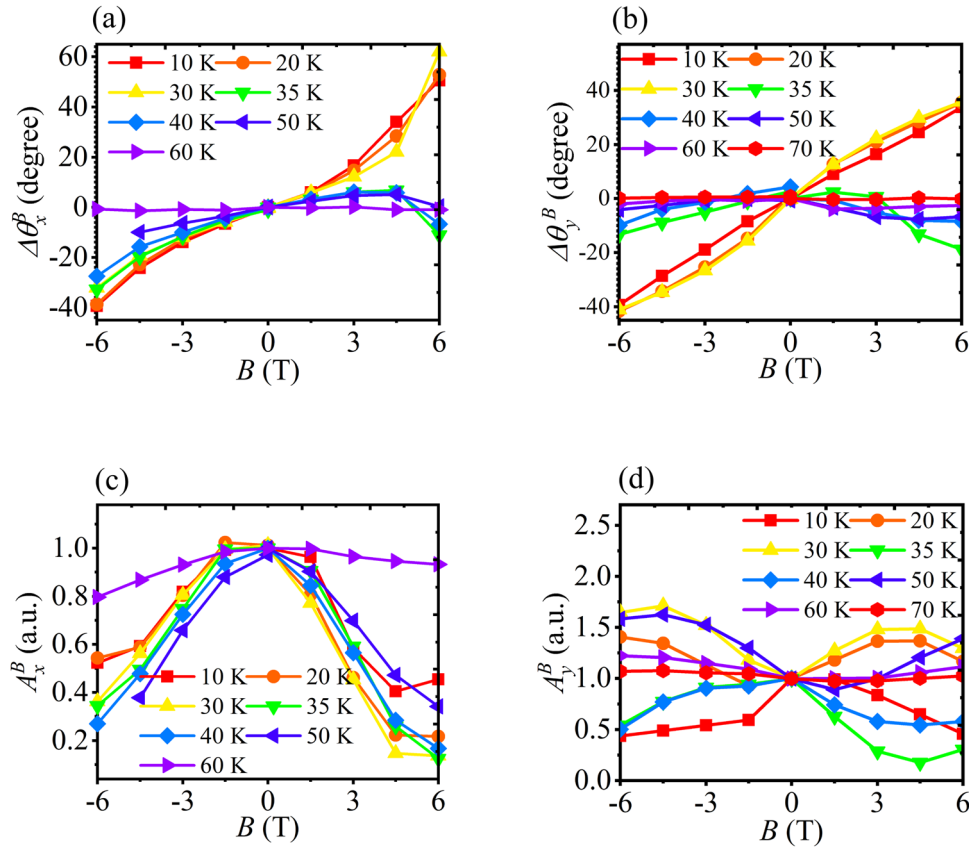


Fig. 2 Magnetic field-dependent bulk photovoltaic (BPV) characteristics at various temperatures (10 K to 70 K). **a** Magnetic field-dependent angle shifts of BPV current along x direction $\Delta\theta_x^B$. **b** Magnetic field-dependent angle shifts of BPV current along the y direction $\Delta\theta_y^B$. **c** Magnetic field-dependent amplitude of BPV current along x direction A_x^B . **d** Magnetic field-dependent amplitudes of BPV current along the y direction A_y^B . The directions x and y are defined in Fig. 1a. The error bars in the plots represent the standard error. The error bars are obtained from the standard deviation of the least-squares fit parameters and are smaller than the points.

$$J_y^{x,B} = \Delta_x^{x,B} J_y^B = \Delta_y^{x,B} A_y \sin(4(\theta + \theta_y)) \quad (7)$$

$$J_x^{y,B} = \Delta_y^{y,B} J_x^B = \Delta_x^{y,B} A_x \sin(4(\theta + \theta_x)) \quad (8)$$

where $J_x^{x,B}$ and $J_y^{x,B}$ are the photocurrents projected from J_x^B on the x and y axis, respectively; $J_y^{y,B}$ and $J_x^{y,B}$ are the photocurrents projected from J_y^B on the x and y axis respectively; $\Delta_x^{x,B}$, $\Delta_x^{y,B}$, $\Delta_y^{x,B}$ and $\Delta_y^{y,B}$ are the corresponding projection coefficients. Summing up two compounds on each axis into the total BPV currents, i.e., J_x^B and J_y^B , we have the modified magnetic field-dependent photocurrents expressed as:

$$J_x^B = J_x^{x,B} + J_x^{y,B} = \Delta_x^{x,B} A_x \sin(4(\theta + \theta_x)) + \Delta_y^{x,B} A_y \sin(4(\theta + \theta_y)) \quad (9)$$

$$J_y^B = J_y^{x,B} + J_y^{y,B} = \Delta_x^{y,B} A_x \sin(4(\theta + \theta_x)) + \Delta_y^{y,B} A_y \sin(4(\theta + \theta_y)) \quad (10)$$

By fitting the magnetic field-dependent BPV currents J_x^B and J_y^B with the initial BPV currents, we obtained the projection coefficients $\Delta_x^{x,B}$, $\Delta_x^{y,B}$, $\Delta_y^{x,B}$ and $\Delta_y^{y,B}$.

The results at 10 K as an example are displayed in Fig. 3c, d. The projection coefficients $\Delta_x^{x,B}$ and $\Delta_y^{y,B}$ have similar features, that is, decreasing by both positive and negative magnetic fields and becoming zero at about 3.5 T. Further increasing the positive or negative field results in the negative values of $\Delta_x^{x,B}$ and $\Delta_y^{y,B}$.

This means that the projection of the rotated photocurrent is oriented in the opposite direction, indicating the magnetic field switches the direction of the photocurrents by more than 90° . On the other hand, $\Delta_x^{x,B}$ and $\Delta_y^{y,B}$ show opposite-sign sinusoidal curves as a function of the magnetic field. The maximum absolute values of both $\Delta_x^{x,B}$ and $\Delta_y^{y,B}$ are situated at $\sim \pm 3$ T. This hints that the maximum projection of photocurrent on the other axis happens at $\sim \pm 3$ T, agreeing with the conclusion for $\Delta_x^{x,B}$ and $\Delta_y^{y,B}$.

Microscopic origin. From the perspective of macroscopic photocurrent, it is clear that a ~ 3 T magnetic field would rotate the photocurrent by 90° in the direction. Alternatively, this can be understood by the picture that the direction of the mean free path of a single carrier is changed by 90° (see Fig. 3e). To understand this process, we consider the Lorentz force as a centripetal force on the moving charged carriers. Thus, we have:

$$e V_{\text{nth}} B = m_e^* V_{\text{nth}}^2 / r \quad (11)$$

$$r = \frac{m_e^* V_{\text{nth}}}{eB} \quad (12)$$

where e is the unit charge, m_e^* is the effective electron mass, r is the effective radius of the circular path, B is the magnetic field, and V_{nth} is the non-thermalised velocity of the carriers. The free path i.e., the mean free path l deflected by the magnetic field is expressed as:

$$l = \text{rad} \times r = V_{\text{nth}} \tau \quad (13)$$

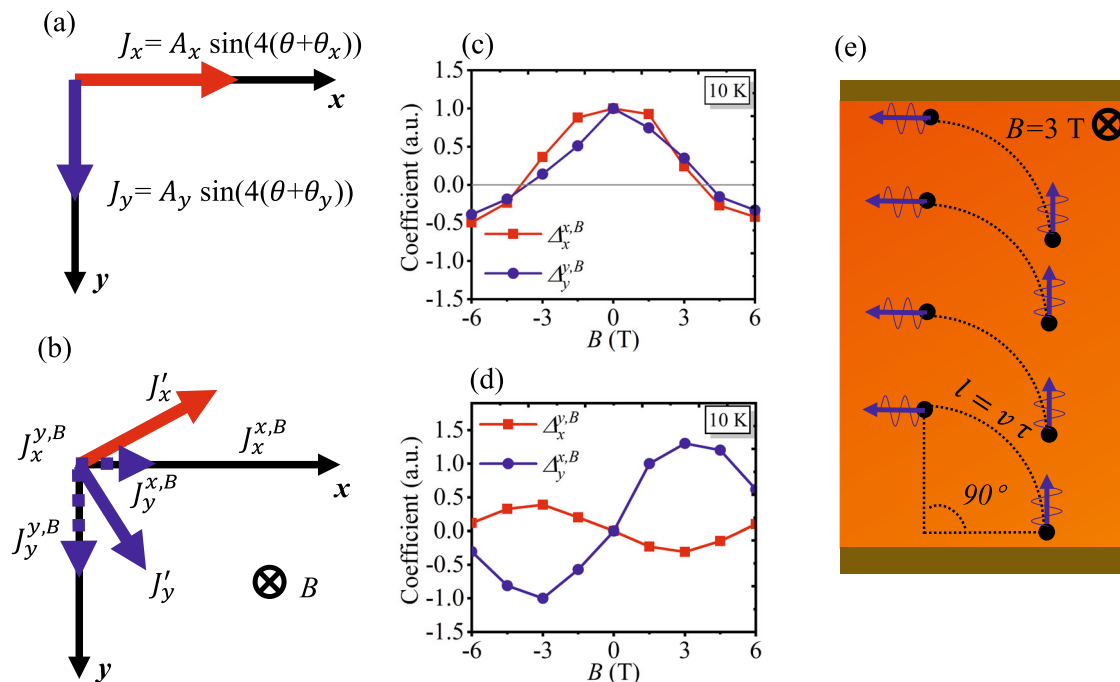


Fig. 3 Macroscopic and microscopic analysis. Schematic illustrations of bulk photovoltaic (BPV) effect **a** without the magnetic field and **b** under the magnetic field \mathbf{B} in the out-of-plane direction. J_x and J_y are the original photocurrents along the x and y directions, respectively. J_x^B and J_y^B are the Lorentz forced-induced photocurrent of J_x and J_y , respectively. $J_x^{x,B}$ and $J_y^{y,B}$ are the photocurrents projected from J_x^B on the x and y axis respectively; $J_x^{y,B}$ and $J_y^{x,B}$ are the photocurrents projected from J_y^B on the x and y axis respectively; $\Delta_x^{x,B}$, $\Delta_x^{y,B}$, $\Delta_y^{x,B}$ and $\Delta_y^{y,B}$ are the corresponding projection coefficients. **c** Magnetic field-dependent projection coefficients of $\Delta_x^{x,B}$ and $\Delta_y^{y,B}$ at 10 K. **d** Magnetic field-dependent projection $\Delta_x^{y,B}$ and $\Delta_y^{x,B}$ at 10 K. **e** Illustration of Lorentz force acting on electrons under a 3 T magnetic field. The direction of the electron's motion is indicated by the blue arrow; the black dashed line indicates the trajectory of the motion of electrons. The error bars in the plots represent the standard error. The error bars are obtained from the standard deviation of the least-squares fit parameters and are smaller than the points.

where rad is the angle rotated by the magnetic field, and τ is the relaxation time of free carriers. By substituting $B = 3$ T and $rad = \pi/2$ into Eq. 13, we have the moment relaxation time $\tau = 3$ ps. In addition, the mobility of non-thermal carriers is also obtained as $\mu_{nth} = B^{-1} \Delta_x^{y,B}$ (or $\Delta_y^{x,B}$) $\approx 3.3 \times 10^3 \text{ cm}^2 \text{ V}^{-1} \text{ s}^{-1}$, much larger than the reported values in other systems¹⁷. It is worth noting that carrier mobility is an innate property of the material and it is not magnetic field dependent.

To further estimate the mean free path of the carriers, the non-thermalised velocity is required as indicated in Eq. 13. To obtain the non-thermalised velocity, one may need to know the exact values of the momentum and energy of the excited carriers¹⁸. Determining these values is, however, beyond the currently available experiments or literature. Anyhow, as the carrier has higher energy in the non-thermalised state than its thermalised state, we can assume that the velocity of non-thermalised carriers is higher than the thermal velocity¹⁹. Therefore, the mean free path value estimated from the thermal velocity will be the lower limit of the actual mean free path. In a two-dimension system, the thermal velocity of the free carrier can be expressed as:

$$V_{nth} = \sqrt{2k_B T / m_e^*} \quad (14)$$

where k_B is the Boltzmann constant. We therefore get $V_{nth} = 1.7 \times 10^4 \text{ m s}^{-1}$ for the free carrier at 10 K. By substituting this value into Eq. 13, we obtain the mean free path $l > 50$ nm.

The above analysis indicates that a magnetic field of $\sim \pm 6$ T would result in the projection coefficient $\Delta_x^{x,B}$ and $\Delta_y^{y,B}$ being -1 as the pristine photocurrents in both two directions should be 180° reversed. While our results show the $\Delta_x^{x,B}$ and $\Delta_y^{y,B}$ are both ~ -0.5 . Therefore, other effects such as the magneto-photovoltaic

effect may also involve and contribute¹¹. The deviation of experimental results from the theoretical prediction is larger at higher temperatures (Supplementary Note 5 and Supplementary Fig. 5). Specifically, when the temperature is at 50 K or higher, the carrier mobility decreases sharply, therefore, the Hall-effect analysis is no longer applicable. These results indicate that the Hall-BPV effect is dominating only in the low-temperature range.

To understand the above characters of the BVP current, we have to invoke the microscopic BPV theory, i.e., ballistic and shift effect^{18,20–23}. These two effects have different transport properties. The shift current has a short relaxation time ($\ll 10^{-14}$ s) which prevents it from responding to the magnetic field^{10,17}, however, the ballistic process has a relatively longer relaxation time which allows the magnetic field via a Lorentz force to effectively act on the carriers over its mean free path^{1,18}. It has been shown that the ballistic effect has a carrier relaxation time in the range of $10^{-14} - 10^{-12}$ s and a mean free path of 10–100 nm, which are in good agreement with our experiments^{1,7}. We further demonstrated that other oxide-STO heterostructures also show the shift of BPV angles in the presence of the magnetic field, indicating the manifestation of the Hall-BPV effect is largely due to the nature of STO (Supplementary Note 6 and Supplementary Fig. 6).

Conclusions

In this work, we have reported a magnetic-field tuned BPV effect in the BFO/STO thin film. By a detailed Hall-effect analysis, we demonstrated that hot photocarriers of the BFO/STO system at low temperatures have transport characteristics within the realm of ballistic transport. We believe this study can not only help to understand the ballistic current but also could be a good example

to obtain the fundamental electronic properties of non-centrosymmetric materials.

Methods

Sample and electrode fabrication. (001)-oriented STO substrates with a 4° miscut along [011]_C direction were used for the deposition of BFO monodomain structures. Before the deposition, STO substrates were etched in buffered oxide etchant for 15 s, and then were annealed in air at 1100 °C for 2 h. BFO monodomain thin films were grown at 650 °C under an oxygen pressure of 0.15 mbar. The pulsed laser energy was set at 0.7 J cm⁻² with a 10 Hz frequency. To conduct the electrical measurements, a pair of ~40 nm thick gold electrodes was fabricated on the top of the surface. The electrodes are in the dimensions of 900 μm × 600 μm and a spacing of 100 μm, running either parallel or perpendicular to the in-plane ferroelectric polarisation as shown in Supplementary Note 1 and Supplementary Fig. 1.

Electrical measurement setup. A homemade optical PPMS was used in this study. Photocurrent characterisation was performed by measuring the in-plane current in two directions under the illumination of a 405 nm (3.06 eV) laser at ~35 mW incident power. A half-wave plate was placed between the sample and the laser source to modulate the polarisation of the light. The rotating rate of the half-wave plate is 2 degrees per second. A high-impedance electrometer (Keithley 6517B) was used to collect the photocurrent in real-time. The magnetic field was applied in the direction normal to the film plane with a sweeping rate of 100 Oe per second. Photocurrents were measured when the system was stabilised for at least 5 mins to avoid any heating or drift effects.

Data availability

The data that support the findings of this study are available from the corresponding author upon reasonable request.

Received: 28 June 2022; Accepted: 2 December 2022;

Published online: 13 December 2022

References

- Sturman, B. I. & Fridkin, V. M. *Fridkin. The photovoltaic and photorefractive effects in noncentrosymmetric materials*. Gordon and Breach Science Publishers (1992).
- Belinicher, V. I. & Sturman, B. I. The photogalvanic effect in media lacking a center of symmetry. *Sov. Phys. Usp.* **23**, 199 (1980).
- Spanier, J. E. et al. Power conversion efficiency exceeding the shockley-queisser limit in a ferroelectric insulator. *Nat. Photonics* **10**, 611–616 (2016).
- Grinberg, I. et al. Perovskite oxides for visible-light-absorbing ferroelectric and photovoltaic materials. *Nature* **503**, 509–512 (2013).
- Bube, R. H. *Photoconductivity of solids*. John Wiley & Sons (1960).
- Alexe, M. Local mapping of generation and recombination lifetime in BiFeO₃ single crystals by scanning probe photoinduced transient spectroscopy. *Nano. Lett.* **12**, 2193–2198 (2012).
- Zenkevich, A. et al. Giant bulk photovoltaic effect in thin ferroelectric BiFeO₃ films. *Phys. Rev. B* **90**, 161409 (2014).
- Shigetomi, S., Ikari, T., Koga, Y. & Shigetomi, S. Photoconductivity and photo-hall effect of p-type InSe single-crystals. *Jpn. J. Appl. Phys.* **20**, L343–L346 (1981).
- Gunawan, O. et al. Carrier-resolved photo-hall effect. *Nature* **575**, 151–155 (2019).
- Burger, A. M. et al. Direct observation of shift and ballistic photovoltaic currents. *Sci. Adv.* **5**, eaau5588 (2019).
- Ivchenko, E. L., Lyandageller, Y. B. & Pikus, G. E. Magnetophotogalvanic effects in noncentrosymmetric crystals. *Ferroelectrics* **83**, 19–27 (1988).
- Burger, A. M. et al. Shift photovoltaic current and magnetically induced bulk photocurrent in piezoelectric Sillenite crystals. *Phys. Rev. B* **102**, 081113 (2020).
- Yang, M. M., Luo, Z. D., Kim, D. J. & Alexe, M. Bulk photovoltaic effect in monodomain BiFeO₃ thin films. *Appl. Phys. Lett.* **110**, 5 (2017).
- Zhang, H. B. & Alexe, M. Optoelectronic functionality of BiFeO₃-SrTiO₃ interface. *Adv. Electron. Mater.* **8**, 2100665 (2022).
- Tufte, O. & Chapman, P. Electron mobility in semiconducting strontium titanate. *Phys. Rev.* **155**, 796 (1967).
- Zhang, H. B., Yang, M. M. & Alexe, M. Boosting the photocurrent in BiFeO₃ thin films via a domain-wall-defect interaction. *Adv. Photonics Res.* 2200189 (2022).
- Gu, Z. Q. et al. Mesoscopic free path of nonthermalized photogenerated carriers in a ferroelectric insulator. *Phys. Rev. Lett.* **118**, 096601 (2017).
- Astafiev, S. B., Fridkin, V. M., Lazarev, V. G. & Shlensky, A. L. Magnetophotovoltaic effect in crystals without a center of symmetry. *Ferroelectrics* **83**, 3–18 (1988).
- Fridkin, V. M., Grekov, A. A. & Rodin, A. I. The bulk photo-voltaic effect in the crystals without a center of symmetry. *Ferroelectrics* **43**, 99–108 (1982).
- Rowley, S. E. et al. Ferroelectric quantum criticality. *Nat. Phys.* **10**, 367–372 (2014).
- Dai, Z. B. et al. Phonon-assisted ballistic current from first principles calculations. *Phys. Rev. Lett.* **126**, 177403 (2021).
- Young, S. M. & Rappe, A. M. First principles calculation of the shift current photovoltaic effect in ferroelectrics. *Phys. Rev. Lett.* **109**, 116601 (2012).
- Young, S. M., Zheng, F. & Rappe, A. M. First-principles calculation of the bulk photovoltaic effect in bismuth ferrite. *Phys. Rev. Lett.* **109**, 236601 (2012).

Acknowledgements

The work was partly supported by the EPSRC (UK) through grant no. EP/T027207/1 and EP/P025803/1.

Author contributions

H.Z. conceived the idea and designed the experiments with M.A.'s supervision. H.Z. grew the thin films, fabricated the devices, and carried out all the electrical measurements. H.Z. and M.A. developed the model and wrote the manuscript.

Competing interests

The authors declare no competing interests.

Additional information

Supplementary information The online version contains supplementary material available at <https://doi.org/10.1038/s42005-022-01108-6>.

Correspondence and requests for materials should be addressed to Hang-Bo Zhang or Marin Alexe.

Peer review information *Communications Physics* thanks Aaron M. Burger and the other, anonymous, reviewer(s) for their contribution to the peer review of this work. Peer reviewer reports are available.

Reprints and permission information is available at <http://www.nature.com/reprints>

Publisher's note Springer Nature remains neutral with regard to jurisdictional claims in published maps and institutional affiliations.



Open Access This article is licensed under a Creative Commons Attribution 4.0 International License, which permits use, sharing, adaptation, distribution and reproduction in any medium or format, as long as you give appropriate credit to the original author(s) and the source, provide a link to the Creative Commons license, and indicate if changes were made. The images or other third party material in this article are included in the article's Creative Commons license, unless indicated otherwise in a credit line to the material. If material is not included in the article's Creative Commons license and your intended use is not permitted by statutory regulation or exceeds the permitted use, you will need to obtain permission directly from the copyright holder. To view a copy of this license, visit <http://creativecommons.org/licenses/by/4.0/>.

© The Author(s) 2022